Principal-Ordinates Propagation for Real-Time Rendering of Participating Media

Oskar Elek[a,b], Tobias Ritschel[a,b], Carsten Dachsbacher[c], Hans-Peter Seidel[a,b]

[a] *Max Planck Institut Informatik*
[b] *MMCI Cluster of Excellence, Saarland University*
[c] *Karlsruhe Institute of Technology*

Abstract

Efficient light transport simulation in participating media is challenging in general, but especially if the medium is heterogeneous and exhibits significant multiple anisotropic scattering. We present Principal-Ordinates Propagation, a novel finite-element method that achieves real-time rendering speeds on modern GPUs without imposing any significant restrictions on the rendered participated medium. We achieve this by dynamically decomposing all illumination into directional and point light sources, and propagating the light from these virtual sources in independent discrete propagation domains. These are individually aligned with approximate principal directions of light propagation from the respective light sources. Such decomposition allows us to use a very simple and computationally efficient unimodal basis for representing the propagated radiance, instead of using a general basis such as spherical harmonics. The resulting approach is biased but physically plausible, and largely reduces the rendering artifacts inherent to existing finite-element methods. At the same time it allows for virtually arbitrary scattering anisotropy, albedo, and other properties of the simulated medium, without requiring any precomputation.

Keywords: participating media; light scattering; natural phenomena; real-time rendering; physically-based rendering; finite elements

1. Introduction

Scattering, or translucency, greatly contributes to the appearance of many natural substances and objects in our surrounding. Albeit the problem can be easily formulated as the radiance transfer equation [3, 23], computing a solution can be very costly. Consequently, many existing approaches simplify the problem, e.g. by assuming isotropic scattering or homogeneity of the material, to achieve interactive performance.

In this work we propose a novel algorithm for plausible real-time rendering of heterogeneous participating media with arbitrary anisotropy. The core of our approach is to propagate light in propagation volumes oriented along the *principal ordinates* of the source illumination. For this we typically use multiple rectilinear grids to propagate environmental (distant) lighting, and spherical grids to account for point light sources. In both cases, one dimension of the grids is aligned with the prominent directional part of the source radiance for which the grid has been created. In contrast to previous methods (e.g. [15, 1]), discretizing the illumination into directional and point light sources enables us to approximately describe the anisotropy (directionality) of light transport by a single scalar value per grid cell. Specifically, this anisotropy value corresponds to a unimodal function implicitly aligned with the respective principal ordinate. In addition to exploiting data locality and the parallelism of GPUs, the benefit of these decisions is a significant reduction of the *false scattering* (numerical dissipation) and *ray effect* (misalignment errors) artifacts arising in many finite-element methods as a consequence of representing the propagated radiance by, e.g. spherical harmonics or piecewise-constant functions. Our main contributions can be summarized as follows:

- We propose the concept of Principal-Ordinates Propagation (POP), a deterministic finite-element scheme suitable for real-time simulation of anisotropic light transport in heterogeneous participating media (Sec. 3).
- The theory of iterative light propagation in a uniform Euclidean grid using a minimal unimodal propagation basis and explicit alignment with the illumination direction to minimize propagation artifacts and maintain light directionality (Sec. 4).
- An extension of the propagation scheme to handle environmental illumination by decomposing it in a set of discrete directions. This includes several new steps, namely specialized prefiltering, importance propagation, and a separate propagation of isotropic residual energy (Sec. 5).
- An extension to local light sources via spherical grids, enabling the integration of instant radiosity to simulate light interaction between solid objects and the medium (Sec. 6).
- Finally we analyse our approach in a number of diverse scenarios, demonstrating its versatility (Sec. 7).

2. Related work

Offline methods. A range of different approaches has been presented to compute solutions to the radiance transport equation for participating environments [3, 23]. However, none of the classic techniques provides a satisfying combination of generality, robustness, and, most importantly in our context, speed. Unbiased Monte-Carlo methods, such as bidirectional path trac-

Figure 1: Dense smoke exhibiting strong multiple anisotropic scattering produced by a steam locomotive under complex environment illumination. Our approach renders it dynamically without any precomputations at 25 Hz (NVidia GeForce GTX 770).

ing [20] and Metropolis light transport [29] usually require a large number of paths to be traced; in particular in dense media with high scattering anisotropy and albedo (like clouds or milk) the computation time increases tremendously. Caching is often used to speed up the computation, e.g. radiance caching [12], photon mapping [14, 13] or virtual point lights [8]. However, these methods typically do not handle highly anisotropic scattering very well, even with recent improvements [27, 28], and their performance is often far from interactive.

Finite-element methods. Finite-element methods, including volume radiosity [33], the discrete ordinates method (DOM) [3], light diffusion [36], and lattice-Boltzmann transport [10] handle highly multiple scattering well. However, in practice they allow only isotropic or moderately anisotropic scattering, and usually suffer from false scattering (smoothing of sharp light beams) and ray effects (selective exaggeration of scattered light due to discretized directions). Light propagation maps [9] significantly reduce the artifacts, but are still limited to rather low scattering anisotropy.

It can therefore be seen that strong scattering anisotropy is one of the main limiting factors for existing methods. This is unfortunate, as most real-world media exhibit relatively high anisotropy (Henyey-Greenstein [11] coefficient $g \approx 0.9$ or more [26]). Although isotropic approximations are acceptable in some cases, this is generally not a valid assumption and one of the primary motivations for our work.

Interactive rendering. Numerous works focus on individual optical phenomena to achieve interactive or real-time performance. These phenomena include light shafts [32, 7], volume caustics [19, 21], shadows [22, 34], and clouds [2]. Various approaches can also be found in visualization literature, e.g. half-angle slicing [17] which empirically computes forward scattering for volume visualization. Sometimes precomputation is used to speed up the rendering of heterogeneous translucent objects [35, 37] or smoke using compensated ray marching [39]. In contrast, we target general multiple scattering in participating media without any precomputation or focus on a particular phenomenon.

We extend the work of Elek et al. [5], building primarily on the concept of DOM [3] and the more recent light propagation volumes [15, 1]. These approaches are attractive for interactive applications as their grid-based local propagation schemes allow for easy parallel implementation on contemporary GPUs. Our work also shares similarities with the finite-difference time domain method [25], however we only consider the radiance amplitude and in general concentrate on efficiency.

Virtually all existing variants or extensions of DOM use a single scene-aligned propagation grid, where every cell stores a representation of the directional radiance function using spherical harmonics (SH) or piecewise-constant functions. This representation is then used to iteratively calculate energy transfer between nearby cells, typically within a local 18- or 26-neighbourhood. However, this representation is only suited for moderately anisotropic scattering at best – especially for anisotropic media under complex (high-frequency) illumination such approach causes prominent ray effects and false scattering artifacts (see [9]). We take a different approach and propose to identify the most important light propagation directions (principal ordinates) in the scene and then use *multiple propagation grids* aligned with these directions, instead of a single one. This enables using a unimodal representation of the angular energy distribution around the principal direction in each grid cell.

3. Principal-Ordinates Propagation

The core idea of our method is to reduce the main drawbacks of previous grid-based iterative methods, namely false scattering and ray effects. These problems stem from the fact that the propagation domain is generally not aligned with the prominent light transport directions. We propose to remedy these issues by using propagation volumes where the propagation domain is explicitly aligned with approximate principal directions of light transport.

Furthermore, we use only a single scalar value per grid cell to describe the local anisotropy of the directional light distribution. In our scheme, we use the well-known Henyey-Greenstein (HG) [11] distribution; the aforementioned value, called the *anisotropy coefficient*, is used to parametrize this distribution. Using principal directions implies that for more complex lighting scenarios we have to use multiple grids that sufficiently

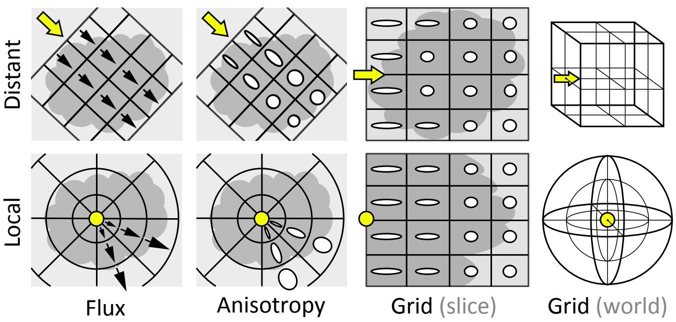

Figure 2: For distant (parallel) light we use rectilinear grids aligned with its principal direction, and spherical grids for point light sources. Every grid cell stores only radiance magnitude and anisotropy. The propagation scheme is almost identical for both cases.

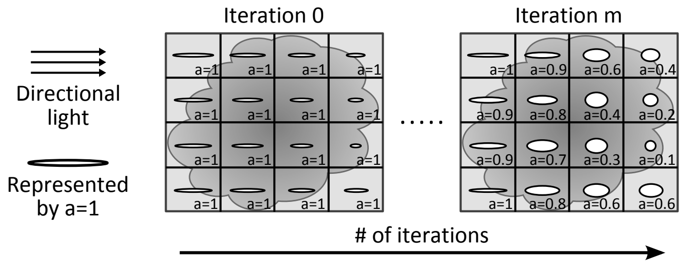

Figure 3: The propagation grid aligned with the direction of incidence is initialized with the attenuated radiance and an anisotropy parameter $a_i = 1$. During the propagation both radiance magnitude and anisotropy change towards lower anisotropy.

well approximate their directionality; for local light sources we propose to use spherical grids centred around them.

These choices inherently assume that the principal directions can be derived from the initial radiance distribution and do not change strongly when light travels through the medium. However, such variation might occur if the density of the simulated medium changes abruptly. Still we deem this to be a necessary compromise if speed is the priority, and as we discuss in Sec. 4.5, violating this assumption does not cause our algorithm to fail, but only leads to a gradual decrease of accuracy.

In the following sections we first detail our concept of Principal-Ordinates Propagation for a single directional source (Sec. 4). Then we describe how to extend this scheme to environment illumination (Sec. 5) and local light sources (Sec. 6) by using multiple, importance-sampled, rectilinear and spherical propagation volumes respectively. The propagation scheme is explained using radiance as the radiometric quantity; we assume all other quantities (such as irradiance from environment maps or intensity from point lights) to be converted accordingly. All frequently-used notation is summarized in Table 1.

4. Rectilinear grids for directional light

The concept as well as the theory behind our propagation scheme can be best explained for parallel (distant) light travelling along a direction $\mathbf{d}$ through a region in space (Fig. 2, top). For this case we discretize the space into a uniform rectilinear grid similar to DOM; however, we make sure that one of its dimensions is aligned with $\mathbf{d}$. For every grid cell i, we store the directional distribution of light and its magnitude L_i (all computations are performed independently per-wavelength, which is omitted here for brevity). The main difference to DOM is that we represent both the *directional distribution* of light and the *phase function* using the HG distribution implicitly aligned with $\mathbf{d}$. To distinguish radiance anisotropy (directional distributions) from phase functions, we denote the HG parameter for the former as $a_i \in [-1, 1]$, and $g \in [0, 1]$ for the latter (we do not consider negative values of g because of physical implausibility of dominantly-backscattering media). That is, the directional radiance of a grid cell centred at $\mathbf{x}_i$ is $L(\mathbf{x}_i, \omega) = L_i \cdot f_{\mathrm{hg}}(\mu, a_i)$, where f_{hg} is the HG function and $\mu = \omega \cdot \mathbf{d}$ is the cosine of the angle between a direction ω and the principal light direction $\mathbf{d}$. We assume that the medium is further characterized by its (spatially-varying) scattering coefficient σ_{s} and absorption coefficient σ_{a}; these two quantities as well as the spatially-varying anisotropy of the phase function defined by the HG parameter g are wavelength-dependent and stored for every cell of the medium volume (which exists *independently* of the propagation volumes).

Conceptually, two grids are required in the propagation procedure. The first, *propagation grid*, stores the unpropagated (residual) energy; we will denote it as $\mathbf{L}$ and its state at the iteration $m \in \{1..M\}$, where M is the total number of propagation iterations, as $\mathbf{L}^m$. The second, *accumulation grid* $\mathbf{L}_{\mathrm{acc}}$, is needed to accumulate the energy transported through the medium over the course of the computation. Two options are available for implementing $\mathbf{L}_{\mathrm{acc}}$: we could either store the overall radiance distribution that has passed though each cell during the propagation, or alternatively store only the observer-dependent out-scattered radiance at each iteration. We opted for the second approach, because storing the entire directional radiance distribution at each cell is much more expensive than just accumulating the outgoing radiance (which is essentially a single scalar value). Although this of course requires recomputing the solution on every observer position change, it is in agreement with our premise of a fully dynamic algorithm without relying on precomputations.

4.1. Grid initialization

At the beginning each propagation grid—which is scaled to span the entire medium (Fig. 2, top)—needs to be initialized by the incident radiance at each cell. As no scattering has been accounted for yet, the anisotropy is set to an HG coefficient of $a_i = 1$, an equivalent to the Dirac function in the direction $\mathbf{d}$ (Fig. 3). That is, for every cell, we compute the transmittance T_i (from the point where light enters the medium, travelling along $\mathbf{d}$ to $\mathbf{x}_i$) set to $L_i = L_{\mathrm{in}}(\mathbf{d}) \cdot T_i$. Note that this can be efficiently computed using ray marching: as our grid is aligned with $\mathbf{d}$ we can compute the transmittance incrementally along individual 'slices' of the grid in a single sweep along $\mathbf{d}$, accessing each cell only once.

$\mathbf{d}$	(principal) direction
g	scattering anisotropy coefficient
σ_s, σ_a	scattering / absorption coefficient
$\mathbf{x}_i$	location of grid cell i
L_i, a_i	(per-cell) radiance magnitude and anisotropy
f_{hg}, F_{hg}	HG function and its cumulative distribution
μ	scattering angle cosine
$\mathbf{L}$, $\mathbf{L}_{\mathrm{acc}}$	propagation and accumulation grid
M, m	number of iterations / iteration index
$L_{\mathrm{in}}(\mathbf{d})$	incident radiance from direction $\mathbf{d}$
$\Delta L_{src\to dst}$	*src* to *dst* radiance contribution
T_i, $T_{src\to dst}$	transmittance to cell i and between cells
Ω_i, Ω_n	solid angle subtended by cell i or ordinate n
N, n	number of principal ordinates / ordinate index

Table 1: Table of frequently-used symbols (in the order of appearance).

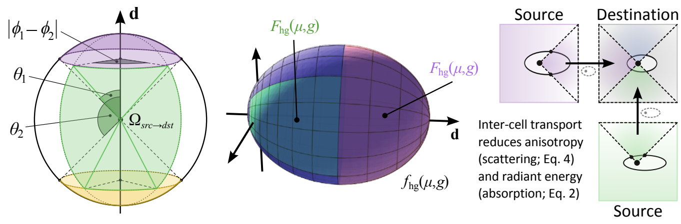

Figure 4: Left: Our polar parametrization of the solid sphere. The coloured patches correspond to the approximate solid angles subtended by the cells next to (green), in front (purple) and behind (orange) *src*. Middle: The HG cumulative function F_{hg} is used to integrate the radiance from the source cell flowing towards the destination cells (depicted as coloured patches of f_{hg}, for $g = 0.5$). Right: On the way the light undergoes scattering and is possibly reduced by absorption.

4.2. Light energy propagation

In this section, we describe how to iteratively update the grid to simulate the propagation of light. We use a propagation stencil where the radiance of each grid cell is propagated to its six direct neighbours in every iteration. Specifically, we perform a more GPU-friendly gathering-type computation of how much radiance flows *into* each grid cell from its neighbours based on their radiance distributions, and then combine these contributions to yield the new distribution at that cell (Fig. 4, right). In the following we denote the neighbouring source cell with index *src*, and the target destination cell with *dst*.

Radiance magnitude contribution. We first need to determine the amount of radiant energy that flows from cell *src* towards *dst* according to the radiance distribution in *src*. To this end, we efficiently integrate $L(\mathbf{x}_{src}, \omega)$ over the solid angle subtended by *dst* (denoted as $\Omega_{src\to dst}$ below) using the closed form of the cumulative HG function $F_{\mathrm{hg}}(\mu, g) = \int_{-1}^{\mu} f_{\mathrm{hg}}(\mu', g)\, d\mu'$:

$$F_{\mathrm{hg}}(\mu, g) = \frac{1-g^2}{4\pi g} \cdot \left(\frac{1}{(1+g^2-2g\mu)^{1/2}} - \frac{1}{1+g} \right). \tag{1}$$

By this we compute the radiance from *src* travelling towards *dst* using the transmittance $T_{src\to dst}$ as

$$\begin{aligned} \Delta L_{src\to dst} = {} & L_{src} \cdot T_{src\to dst} \cdot |\phi_1 - \phi_2| \\ & \cdot \left(F_{\mathrm{hg}}(\cos\theta_1, a_{src}) - F_{\mathrm{hg}}(\cos\theta_2, a_{src}) \right) \end{aligned} \tag{2}$$

using the following approximate parametrization for the subtended solid angle $\Omega_{src\to dst}$ (depending on mutual positions of *src* and *dst*):

$$(\theta_1, \theta_2, |\phi_1 - \phi_2|) = \begin{cases} (0, \frac{\pi}{4}, 2\pi) & dst \text{ in front of } src \\ (\frac{\pi}{4}, \frac{3\pi}{4}, \frac{\pi}{2}) & dst \text{ next to } src \\ (\frac{3\pi}{4}, \pi, 2\pi) & dst \text{ behind } src \end{cases} \tag{3}$$

(see Fig. 4, left for a sample illustration of the second case of Eq. 3). Since the HG distribution is rotationally-symmetric (Fig. 4, middle) only the absolute value of the difference of the azimuthal angles $|\phi_1 - \phi_2|$ is required. Note that here the transmittance $T_{src\to dst}$ accounts *just for absorption* that affects the radiance propagation on its way from *src* to *dst*. This is because our scheme treats scattering as a decrease of anisotropy and not as an extinction process, as we show below. In practice, we take the averaged absorption coefficients σ_{a} at the source and destination cells and the distance between their centres t, and apply the Beer-Lambert-Bouguer law. To avoid aliasing if the resolution of the propagation grid is much smaller than the medium volume resolution, the medium parameters need to be sampled from a downscaled version of the volume. On GPU, downscaling is a very fast operation, as it corresponds to building a small number of MIP map levels (depending on the ratio between the grid resolutions, but usually 1 or 2).

Radiance anisotropy contribution. Similarly to absorption attenuating the radiant energy flowing between neighbouring cells, the anisotropy of the energy propagated from *src* to *dst* will decrease due to scattering. In agreement with the radiance transfer equation, in our case this can be easily computed exploiting the self-convolution property of the HG distribution [24]: in a medium with scattering anisotropy of g the radiance anisotropy reduces to $a' = a \cdot g^{\sigma_{\mathrm{s}} \cdot t}$ after travelling a distance t (assuming a constant σ_{s} along this path). We obtain σ_{s} and t the same way as for computing $T_{src\to dst}$ above. The change of radiance anisotropy from *src* to *dst* is therefore

$$\Delta a_{src\to dst} = a_{src} \cdot g^{\sigma_{\mathrm{s}} \cdot t}. \tag{4}$$

We can easily see that this formula cannot lead to an increase of anisotropy, since $g \in [0, 1]$. Additionally, in non-scattering media ($\sigma_{\mathrm{s}} = 0$) the directionality will be preserved perfectly.

Combining contributions from neighbours. Updating the radiance distribution at the cell *dst* entails accumulating the contributions from its six neighbours (indexed by *src*) as

$$L_{dst} = \sum_{src} \Delta L_{src\to dst}, \tag{5}$$

$$a_{dst} = \frac{\sum_{src} \Delta L_{src\to dst} \cdot \Delta a_{src\to dst}}{\sum_{src} \Delta L_{src\to dst}}. \tag{6}$$

While the radiant energy contributions simply need to be added up, the anisotropy is a weighted average of its neighbours, since the update has to yield an anisotropy value a_{dst} within the valid range. We discuss implications of Eq. 6 in Sec. 4.5.

4.3. Iterating the solution

The update procedure defined by Eqs. 5 and 6 is performed for every cell of $\mathbf{L}^m$ to yield $\mathbf{L}^{m+1}$ for every iteration m. Implementation-wise, this requires maintaining a second grid identical to the propagation grid and swapping these at each iteration.

Additionally, the results of every propagation iteration need to be accumulated in $\mathbf{L}_{\text{acc}}$ by evaluating the updated distributions in $\mathbf{L}^{m+1}$:

$$L^{m+1}_{\text{acc},i} = L^{m}_{\text{acc},i} + L^{m+1}(\mathbf{x}_i, \mathbf{c} - \mathbf{x}_i) \quad (7)$$

$$= L^{m}_{\text{acc},i} + L^{m+1}_i \cdot f_{\text{hg}}(\mu, a^{m+1}_i) \quad (8)$$

for every cell i. Here $\mathbf{c}$ is the observer position and μ is therefore the dot product of $\mathbf{d}$ and the view direction.

4.4. Upsampling and rendering

When the solution has converged after a sufficient number of iterations, using it for rendering is relatively straightforward. We employ ray-marching to integrate the incoming radiance for every camera ray using the common front-to-back emission-absorption model [23]. In this case the emission term corresponds to the scattered radiance accumulated in $\mathbf{L}_{\text{acc}}$.

As we discuss in Sec. 7, the typical resolutions used for the propagation grids need to be rather small (in most of our examples 20^3 or less) for performance reasons. In order to improve the rendering quality with such low grid resolutions it is desired to upsample them prior to their visualization. We use a 3D version of the joint bilateral upsampling [18] where the density field of the medium (i.e. the spatially varying scattering coefficient) is used as a guidance signal. Typically, the density field is significantly more detailed than the propagation volumes; this detail is "transferred" to the solution by the upsampling. According to our experiments, low-resolution propagation grids are usually sufficient for plausible results.

4.5. Discussion of the propagation scheme

Using the unimodal HG function with a single parameter to represent the directional distributions in light transport obviously means that there are distributions in a cell that cannot be represented well. On the other hand, we compensate for this by using multiple grids (see Sec. 5), which in turn can handle anisotropic phase functions significantly better than previous work thanks to the proposed propagation scheme. In comparison, an exceedingly large number of SH coefficients is required to represent highly anisotropic distributions, and this still does not prevent false scattering issues if a local propagation scheme is employed.

The most heuristic step of our scheme is the recombination of reduced anisotropies from neighbouring cells in Eq. 6 (which we further elaborate on in the supplementary materials). The logic behind this formulation is that the radiance distribution

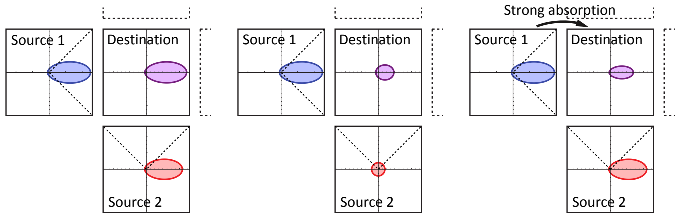

Figure 5: Three examples of the local propagation behaviour. Left: all source cells exhibit strong forward scattering which is well-preserved by our propagation scheme. Centre: radiance anisotropy is reduced due to in-scattering from Source 2 which has isotropic radiance distribution. Right: light from Source 1 to destination is almost entirely absorbed. Light from Source 2 should then be deviated "upwards", which our scheme cannot represent.

at *dst* will result from superposing the neighbouring distributions according to how much energy they contribute to *dst*. The main limitation of this approach lies in the fact that combining multiple HG distributions with different anisotropy values cannot generally be represented by any single HG distribution. Although we have experimented with fitting the resulting HG distribution to the combination of its neighbours in terms of least square error, we found that the simple weighted arithmetic average produces comparable results while keeping the computational cost of this core operation minimal. In addition, Eq. 6 very well preserves the anisotropy of light transported along the principal direction, thus greatly reducing false scattering effects.

Note that there are cases of very heterogeneous media where our approach might locally become inaccurate (see Fig. 5). If light along the principal direction undergoes strong absorption, while light from other directions does not, the resulting light distribution should possibly become skewed, which cannot be represented within our framework. Although this is obviously a failure case of our representation, occurrences of such strong absorption fluctuations are comparatively rare, and more importantly the resulting radiance magnitude in these cases is typically very small (therefore having little impact on the resulting image). Also note that with multiple propagation volumes we can actually reproduce complex multimodal radiance distributions, despite each grid being composed of unimodal HG distributions.

5. Multiple propagation grids for environment lighting

In the previous section we have described our approach for a single directional light source. In order to account for environmental lighting (typically modelled by an environment map), we need to use multiple grids oriented along different principal directions.

In this section we discuss how to choose these directions and, as every grid accounts for light from a finite solid angle, how to prefilter the respective incident radiance to avoid singularity artifacts (see Fig. 6). We further describe how the multiple propagation grids are combined together for rendering. Finally we present an additional (optional) step in the pipeline of our algorithm, which allows splitting the propagation into two stages,

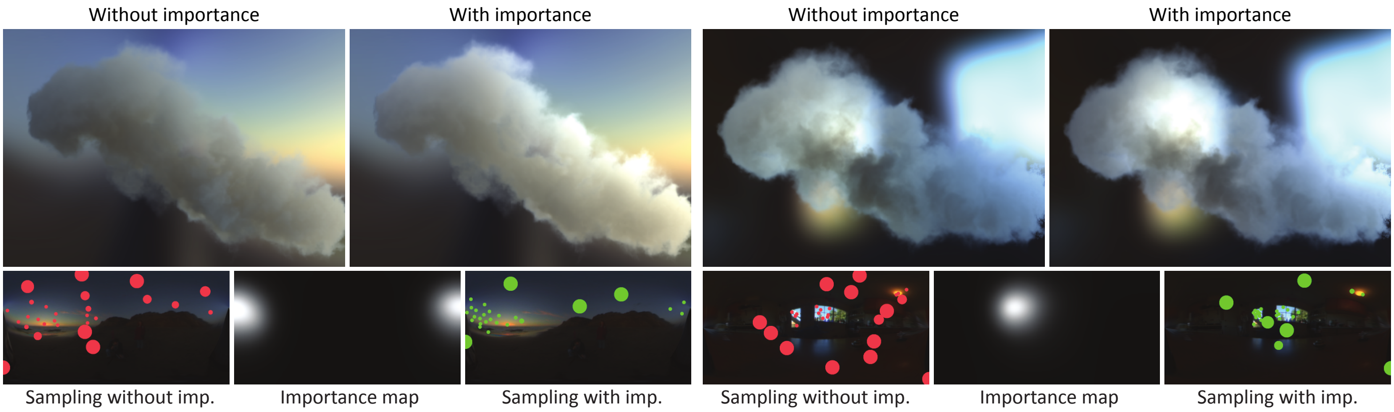

Figure 7: Importance propagation improves overall radiance distribution across the medium and visibility of bright regions behind. This especially holds for high-albedo media with strong scattering anisotropy (here $g = 0.98$) and when using a low number of ordinates (27 here).

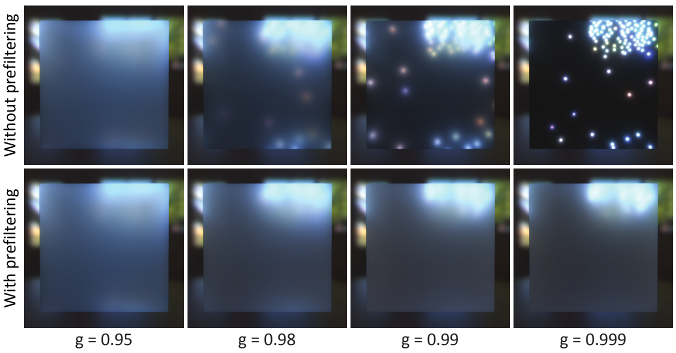

Figure 6: The effect of prefiltered initialization on a thin, strongly-scattering medium with increasing anisotropy (left to right). Without prefiltering (top) the individual ordinates become apparent. Using prefiltering (bottom) the resulting images become much smoother and yield the expected appearance (more anisotropic slabs appear more transparent). Note that our technique is energy-conserving (as opposed to, e.g. singularity clamping in instant radiosity).

anisotropic and isotropic, greatly improving the convergence for media with very high albedo values.

5.1. Prefiltering

A straightforward approach is importance-sampling the environment map to obtain N directions, $\mathbf{d}_n$, each carrying an energy corresponding to its associated portion of the directional domain Ω_n. We can account for the shape of Ω_n when determining the initial directional radiance distributions (parameter a_i in Sec. 4.1). Recall that the anisotropy parameter of f_{hg} represents the average cosine of the distribution. We can therefore approximate the initial $a_{n,i} = \int_{\Omega_n} -\mathbf{d}_n \cdot \omega \, \mathrm{d}\omega / ||\Omega_n||$, the average cosine between $\mathbf{d}_n$ and the directions in Ω_n and use this value for the grid initialization. In practice, $a_{n,i}$ can be approximated without the integration over Ω_n for each ordinate or without even knowing the shape of Ω_n. As we importance-sample the environment map, the importance of the ordinate n is proportional and (up to a factor) very similar to the actual solid angle of Ω_n. Therefore, we use a heuristic that maps the importance $w_n \in (0,1)$ to anisotropy as $a_{n,i} = (1 - w_n/N)^{\beta}$: important ordinates are denser in the directional domain and will have small solid angles and high anisotropy, while less important ordinates are more sparse, and will have larger solid angles and low anisotropy. The scalar factor $\beta > 0$ defines the proportionality and currently needs to be tuned empirically once for each environment map; from our experience this is a simple and quick task.

5.2. Importance propagation

The described sampling scheme can be further improved by considering how much illumination from different directions actually contributes to the image. To this end, we introduce an additional *importance propagation* step before sampling the environment map: we use a regular grid (perspective-warped into the camera frustum and oriented along the view direction) and propagate importance from the camera through the medium. Thanks to the duality of light transport this is equivalent to the radiance propagation as described before. The result of this propagation is a directional importance distribution stored in the grid cells. By ray-marching this grid we project the importance into the directional domain and create a directional *importance map* that aligns with the environment map. We then sample the environment map according to its product with the importance map. We show that in certain situations this step improves the sampling result, mainly when a low number of propagation grids is used (see Sec. 7 and Fig. 7). It is also quite cost-effective, since the directional importance function is typically very smooth and therefore only low resolutions for the propagation grid and the directional map are required (all our examples use the resolutions of 16^3 and 32×16 respectively).

5.3. Merging multiple grids

Computing the propagation for each of the N principal ordinates yields a separate, view-dependent accumulation grid $\mathbf{L}_{\text{acc},n}$ (Sec. 4). Although it is possible to visualize these directly, this is very inefficient as each grid in the set would have to be accessed at every ray-marching step.

Because of this we instead opt to combine all $\mathbf{L}_{\text{acc},n}$ into a single medium-aligned grid, prior to upsampling and visualization

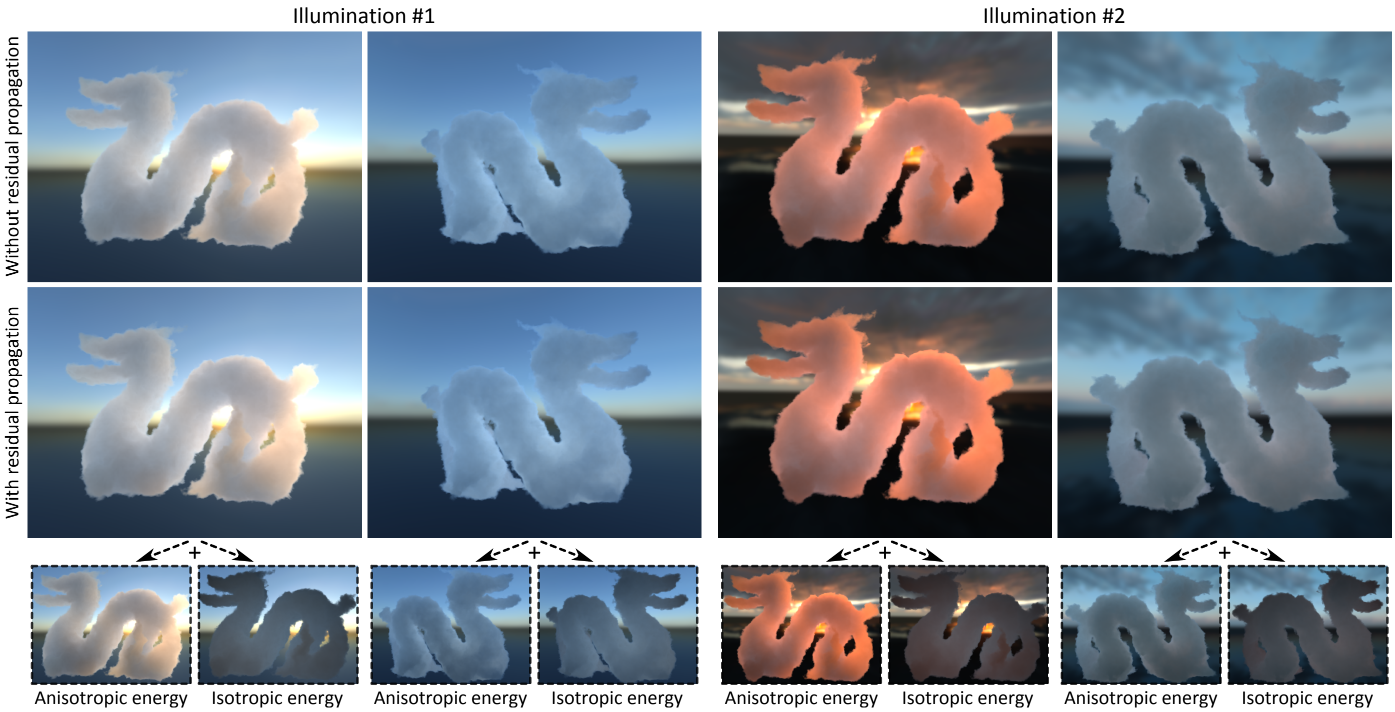

Figure 8: Evaluation of the isotropic residuum (IR) propagation. We show the dragon dataset illuminated by two different environment maps, from two opposing viewpoints for each to demonstrate the view dependence of the resulting light distributions. The used medium (milk [26], $\sigma_s = \{0.91, 1.07, 1.25\}\,\mathrm{m}^{-1}$, $g = 0.95$) has an albedo over 99.9 % across the visible spectrum, making it a difficult material to render because of the high number of iterations necessary to converge. The full propagation (64 ordinates, 16^3 grid each) requires about 100 iterations to converge, taking 120 ms (#1) and 90 ms (#2) respectively. In comparison, our heuristic (Eq. 6) switches to isotropic propagation after $m' = 20$ full anisotropic iterations ($\varepsilon_\mathrm{a} = 0.1$, $\Delta x = 0.25\,m$). The IR propagation requires additional 20 iterations in a single 32^3 propagation grid. The combined propagation time in this case was 28 ms (25 ms anisotropic and 3 ms isotropic) for illumination #1 and 24 ms (20.5 ms anisotropic and 3.5 ms isotropic) for #2; this is about a 4-fold speed-up compared to the full propagation, with negligible visual difference.

(Sec. 4.4). We usually use double the resolution of the individual propagation grids, since these are oriented arbitrarily in space (and therefore not increasing the resolution would result in undersampling). This is however still a very fast step that also allows the remainder of the pipeline to stay virtually identical to the single-ordinate setting.

5.4. *Isotropic residuum*

We assume the solution to be converged when all $\mathbf{L}_n^m$ are below a small threshold ε_L. This can however take a large number of iterations for high-albedo media, a problem inherent to all finite-element transport methods. On the other hand, we can observe that scattering reduces the anisotropy of the radiance distribution and we can treat the propagation as (near-)isotropic as soon as $|a_{n,i}| < \varepsilon_\mathrm{a}\ \forall i, \forall n$, for a small anisotropy threshold ε_a.

As soon as all propagation grids fulfil this criterion the energy from them can be merged into a single grid aligned with the medium, as there is no directionality present anymore. This is similar to merging the accumulation grids (Sec. 5.3), except that here the propagation grids are merged as well and the propagation process switches to isotropic scattering (i.e. the anisotropies $a_{n,i}$ need not be maintained anymore). This decreases the propagation costs tremendously, as from this point it is performed just for a single global grid instead of one grid per principal ordinate.

In practice, we determine the iteration m' when we can switch to the cheaper isotropic propagation based on the maximum radiance anisotropy, $\widehat{a}$ (for a directional light $\widehat{a} = 1$, but prefiltering can lower it, to our benefit), and phase function anisotropy g. Both of these parameters are determined at the initialization. Making use of the the HG self-convolution property (Sec. 4.2), from these values we can approximate the distance t that light has to travel such that its anisotropy falls below ε_a with

$$\widehat{a} \cdot g^{\overline{\sigma}_\mathrm{s} \cdot t} = \varepsilon_\mathrm{a}, \tag{9}$$

where $\overline{\sigma}_\mathrm{s}$ is the average scattering coefficient in the medium. Furthermore, we know that the travel distance depends on the average grid spacing Δx and the number of iterations, i.e. $t = m \cdot \Delta x$, and obtain:

$$m' = \frac{\ln \varepsilon_\mathrm{a} - \ln \widehat{a}}{\ln g} \cdot \frac{1}{\overline{\sigma}_\mathrm{s} \cdot \Delta x}. \tag{10}$$

It is however usually a good idea to use m' at least equal to the grid resolution along the propagation direction, to allow for light even from the first row of cells to sufficiently penetrate into the rest of the volume (cf. [15]). The subsequent propagation then operates on the residual isotropic radiance in the merged grid, iterating until the residual energy falls below ε_L.

Reasonable values for ε_a are around 0.1, or even higher. In fact this decision is not unlike the one made in similarity theory [38].

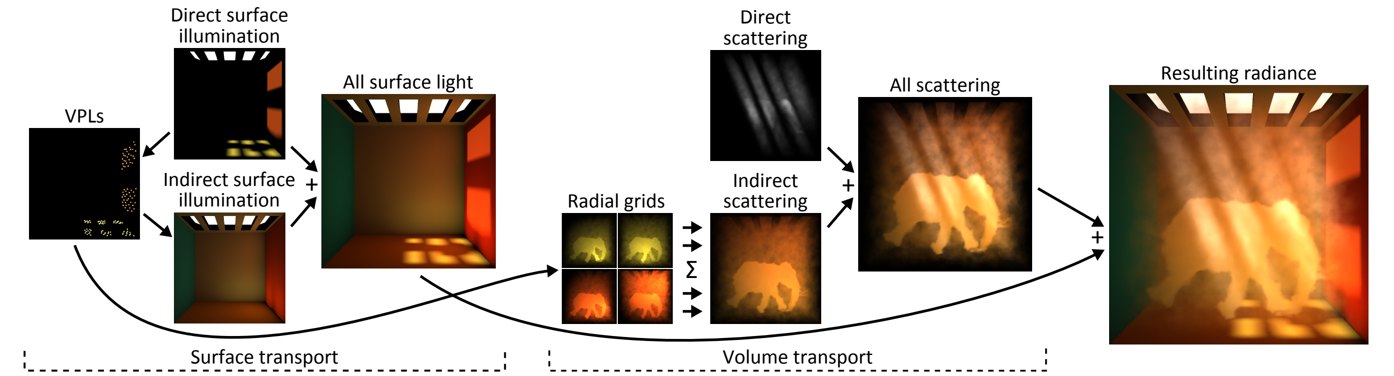

Figure 9: Workflow of the presented algorithm for a single directional light. For distant environment illumination the volumetric part of the pipeline is very similar, with the exception of rectilinear grids being used to propagate illumination from distant ordinates instead of the combination of VPLs and spherical grids.

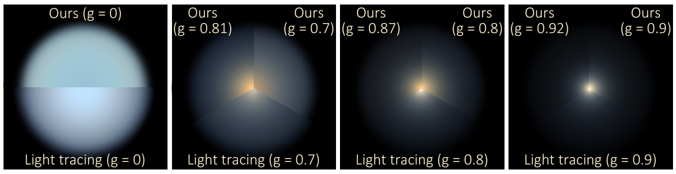

Figure 10: Comparison of our radial propagation to a Monte-Carlo reference for a uniform spherical medium (radius 2.5 m, $\sigma_s = \{0.8, 1, 1.3\}\,\mathrm{m}^{-1}$ and unit albedo). The resolution of the radial propagation grid was 32^3. Our solution differs from the reference mainly due to low (but for this propagation type still present) false scattering, in particular with low anisotropy values. We found that this can be reduced by artificially increasing g, if a specific appearance is desired.

Here, after a certain number of scattering events the propagation switches to isotropic scattering, which is accompanied by a switch to a so-called *reduced scattering coefficient*. This is usually done on an empirical basis and despite the fact that using the Henyey-Greenstein phase function allows us to quantify the decision better (cf. [6]) this approach is still an approximation. Similarity theory also does not apply well to heterogeneous media. Thanks to the fact that we treat scattering as a gradual decrease of anisotropy we can transit to isotropic propagation in a well controlled manner, without changing the propagation parameters or compromising the solution accuracy (aside from small geometric misalignments caused by the grid merging). We demonstrate this in Fig. 8.

6. Radial grids for local light sources

In order to extend our method to local light sources, we use spherical grids with two angular coordinates and a radial coordinate which is again aligned with the initial principal directions of the point source (Fig. 2, bottom). To obtain more isotropic cell shapes, the spacing of shells along the radial coordinate grows exponentially (in proportion to the radial segment length at a given radius). For parametrizing the spherical domain we use the octahedron parametrization [30] mainly as it is simple, provides reasonably uniform sampling, and above all, it discretizes the domain into a 2D square where every cell has four natural neighbours (plus two along the radial axis), similar to rectilinear grids. The resulting grid is thus topologically equivalent to rectilinear grid (except for being cyclic in the two angular dimensions) and albeit not being uniform, it allows us to approximately treat the space as locally Euclidean and obtain plausible results again using virtually the same propagation scheme as before. The main difference in the propagation is that we have to account for the quadratic fall-off : although we base our propagation on radiance, we have to explicitly compensate for the varying grid cell sizes resulting from the non-uniform shell spacing. To this end, we scale the radiance when propagating along the principal direction in proportion to the radial coordinate spacing. A sample demonstration of this propagation type for a point light in a simple homogeneous spherical medium is shown in Fig. 10.

Instant radiosity. Given the ability to use local point lights, we can use instant radiosity [16] methods, which represent complex illumination as a collection of point lights, to simulate surface-to-volume light transport. Normally these VPLs are obtained from random walks through the scene. In our interactive setting, we generate VPLs using a reflective shadow map (RSM) [4] for every primary light. We importance-sample these RSMs according to surface albedo and (attenuated) irradiance, aiming at keeping the total number of VPLs low. The reflected radiance is then used to initialize the radial propagation grids. Prefiltering can be done in the same way as for environment maps: VPLs with a large importance have a high initial anisotropy and vice versa. Similar to surface lighting, we can use clamping to reduce any remaining singularities [8]. Fig. 9 depicts the pipeline of the algorithm when propagating scattering from one directional light and VPLs generated from its RSM.

7. Results and analysis

All results were computed on a PC with a 3.7 GHz Intel Xeon CPU, 16 GB of RAM and an NVidia GeForce GTX 770 GPU with 2 GB of VRAM. Our implementation is written in C++, using OpenGL and GLSL for the GPU code. In all our measurements we use the framebuffer resolution of 800×600 in order to let the computation time be dominated by the propagation rather than ray-marching. Resolutions of the medium density

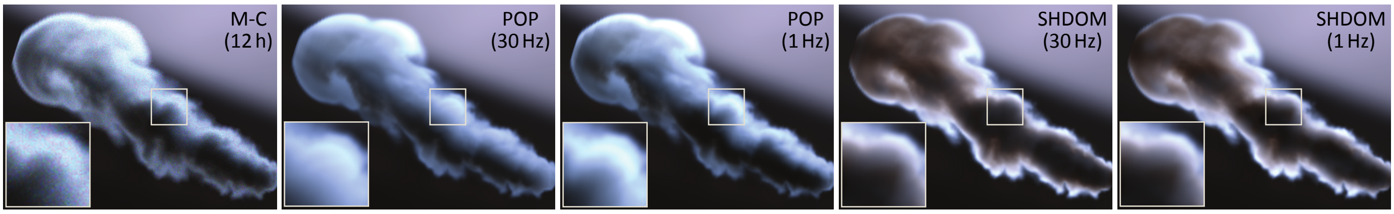

Figure 11: Comparison of our Principal-Ordinates Propagation (POP) to SHDOM and a Monte-Carlo reference (light tracing), for a smoke plume 10 m across with $\sigma_s = \{2.9, 3.6, 4.2\}\,\mathrm{m}^{-1}$, $\sigma_a = \{3.4, 3.35, 3.4\}\,\mathrm{m}^{-1}$ and $g = 0.9$ using the "Uffizi" environment map as illumination. For POP we used 64 and 125 principal ordinates, grid resolutions of 20^3 and 50^3, 10 and 30 propagation iterations, respectively. For SHDOM we have used 5 and 10 bands to represent the directional radiance distribution in each cell and the same grid resolutions. SHDOM required a strong prefiltering to avoid ringing and due to false scattering it fails to reproduce the high scattering anisotropy. Our method compares well to the reference solution, and even with real-time settings it qualitatively matches the overall appearance.

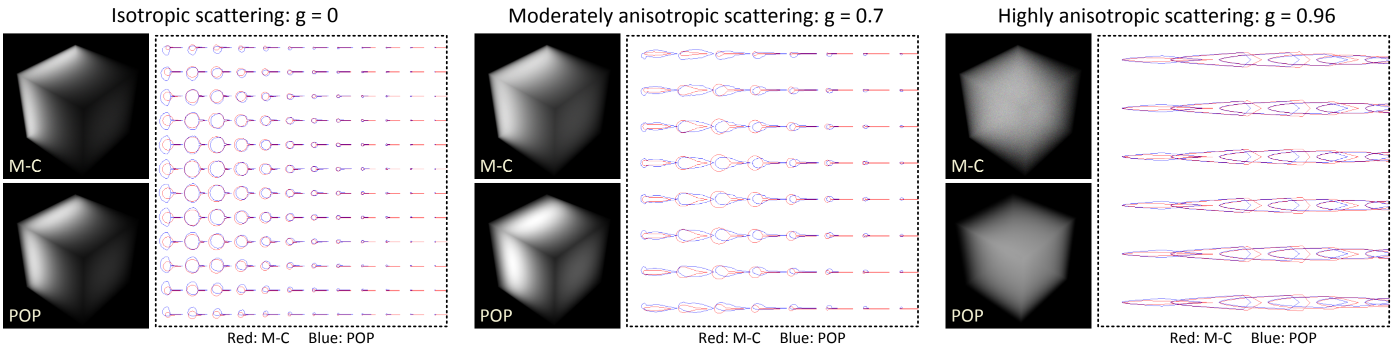

Figure 12: Detailed analysis of our method (POP) in comparison to Monte-Carlo reference (light tracing). We use a sample single-ordinate scenario, with a 16^3 propagation domain aligned with the medium (unit homogeneous cube, $\sigma_s = 4\,\mathrm{m}^{-1}$, 100 % albedo), using three representative anisotropy values. The plots compare the converged (incident) radiance distributions within a 2D horizontal slice in the middle of the domain.

datasets are typically in the order of tens in each dimension (but effectively enhanced by procedural noise). Although the number of propagation iterations needs to be chosen empirically at the moment, in general we found that amounts similar to the propagation grid resolution along the propagation dimension is sufficient (around 10–20 in our examples). Please note that we blur the environment maps only for presentation purposes (so that the medium lighting features can be examined better) – the actual illumination is in fact sampled from the full-resolution maps. Other specific scene details are provided in the caption of each discussed figure.

Reference comparisons. We first compare our approach to an unbiased Monte-Carlo reference (light tracing), as well as spherical harmonics (SH) DOM, in Fig. 11. It is apparent that the described artifacts prevent SHDOM from handling anisotropic media correctly, despite being theoretically capable to do so. In contrast POP, despite being biased, reproduces the qualitative appearance well.

A simpler analysis for a single directional propagation is presented as well. Fig. 12 shows comparisons to the reference for a single ordinate, propagating in a simple cubic medium. Again, despite some differences in the appearance, we can see the directional radiance distributions match well. We note that this is actually a difficult case for our method, because the medium regularity and the high density gradient on the faces parallel to the propagation direction violate the alignment assumption, as discussed in Sec. 4.5. However, observe that the directional distributions produced by POP have more complex shapes that the simple Henyey-Greenstein ellipsoid lobes, since they are constituted by a superposition of such lobes. In addition, Fig. 10 shows a simplified analysis similar to this, for a point light source.

Propagation behaviour. We examine the convergence of our method in Fig. 13. The setting is identical to the second case in Fig. 12. Notice that because of an absence of absorption the propagation takes a significant number of iterations, even for the small 16^3 grid. That is the main motivation for introducing the isotropic residuum propagation (Sec. 5.4).

The effect of using different numbers of principal ordinates is shown in Fig. 14. It can be seen that the discretization becomes apparent only with very few ordinates. The importance propagation usually helps to alleviate this by sampling those directions which will influence the solution most significantly. As Fig. 7 demonstrates, this is most likely the opposite side of the medium, suggesting that a simpler empirical heuristic could potentially work in certain cases.

One of the main shortcomings of the importance propagation is its potential temporal incoherency, mostly manifested by temporal flickering. For this reason we filter the importance map both spatially and temporarily, which, however, is not a fully robust solution to the issue. One of our main targets for future work is therefore improving this by explicitly enforcing temporal coherence when the sampled light sources relocate due to camera movement or illumination changes, similarly to, e.g. [31].

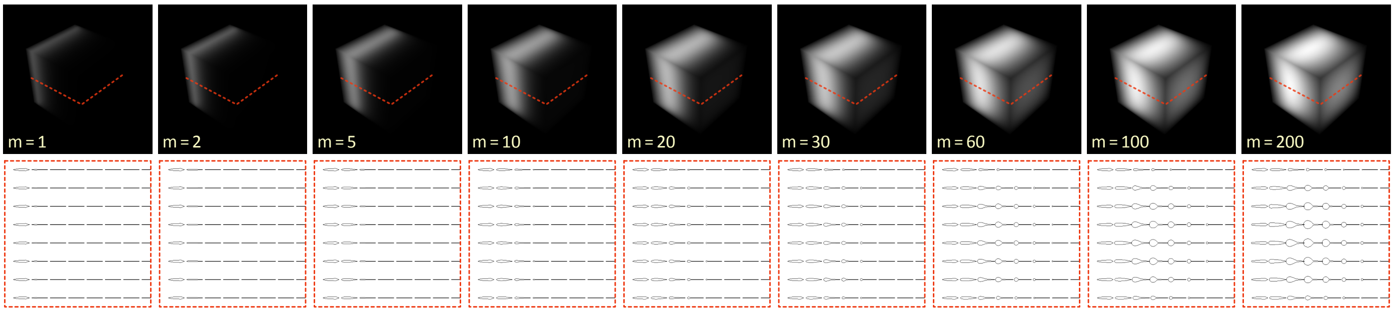

Figure 13: Convergence of our propagation scheme for the setting described in Fig. 12, with scattering anisotropy $g = 0.7$. The plots show the respective incident radiance distributions within a 2D horizontal slice in the middle of the domain (marked by the red dashed line). The observed strong forward peaks represent the *unscattered* energy which did not (yet) interact with the medium.

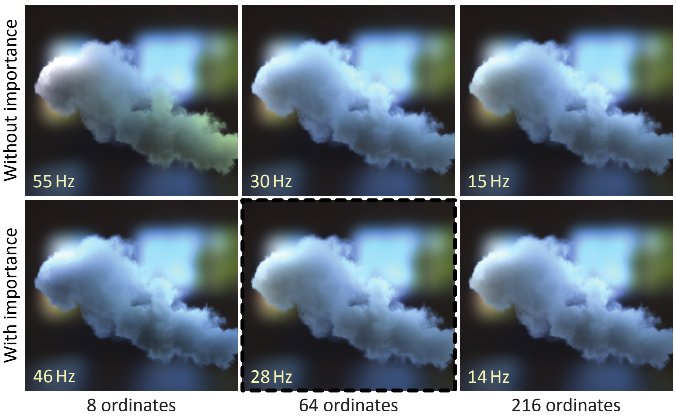

Figure 14: The smoke dataset with an increasing number of ordinates using the "kitchen" environment map ($g = 0.9$, 20^3 grid resolution, 10 propagation iterations). Accounting for importance improves the results, mainly if low numbers of principal ordinates are used. The typical setting we use (shown in the bottom-centre) takes 5 ms for importance propagation, 2 ms for determining the ordinates, 2 ms for grid initialization, 12 ms for propagation, 2 ms for residuum propagation, 4 ms for grid merging and upsampling and 5 ms for ray-marching.

Prefiltering helps to improve the rendering quality in most scenarios and we used it to generate all results throughout the paper. It is particularly indispensable for media with an optical thickness insufficient to blur the sampled illumination, e.g. as in Fig. 6, where singularity-like artifacts would appear otherwise. Our prefiltering removes these artifacts but still allows perceiving features of the background illumination, thanks to its adaptivity (as opposed to a naïve prefiltering of the source illumination).

Scattering anisotropy. The shortcomings of current methods in handling highly anisotropic scattering were the main motivation for our work, as by far the majority of both natural and artificial media exhibit anisotropic scattering (cf. [26]).

We tested our method for clouds with naturally very high scattering anisotropy in comparison to their isotropic versions (Fig. 15). It can be seen that our propagation scheme handles both cases well, and that correctly handling anisotropic scattering is a key to reproducing such media. The same can be observed in Fig. 1, since steam has properties similar to clouds. Interestingly, grid resolutions as well as computation times required to render plausible participating media are rather insensitive to its anisotropy, i.e. anisotropic media render roughly as fast as isotropic media. Although a larger number of ordinates might be required to reproduce high-anisotropy effects, this additional effort is usually compensated by a decreased complexity of the spatial radiance distribution, which enables using coarser propagation grids.

Our dual propagation scheme also efficiently handles optically thick anisotropic media, as seen in Fig. 8. The initial, full propagation handles the directionally-dependent portion of radiant energy, while the remaining isotropic residuum is rapidly propagated in the second stage.

Animation. Thanks to the fully dynamic nature of our approach we can seamlessly handle animated media without any precomputations or performance penalty. Fig. 16 shows several frames of an animated smoke plume coherently rendered at real-time framerates. In Fig. 17 we then demonstrate the dynamic interaction of POP with surfaces, as described in Sec. 6.

In general, we believe to have demonstrated the versatility of our method. Our propagation is capable of computing direct illumination and low-order scattering effects (light shafts), as well as arbitrary multiple scattering from directional, local and environment illumination. Orthogonal to this, POP is capable of simulating media with wide ranges of optical thickness, albedo and most importantly, scattering anisotropy.

8. Discussion and conclusion

We propose a novel discrete ordinates method capable of computing light transport in heterogeneous participating media exhibiting light scattering of virtually arbitrary anisotropy. The method does not require any precomputations, which makes it well suitable for simulating dynamic and evolving media without extra considerations. Our representation also adapts to and prefilters the incident lighting. Radiance is represented by the Henyey-Greenstein distribution, and propagated by our novel scheme in volumes oriented along estimated principal light directions.

In general the steps of the proposed method are physically-plausible (please refer to the supplementary materials for further

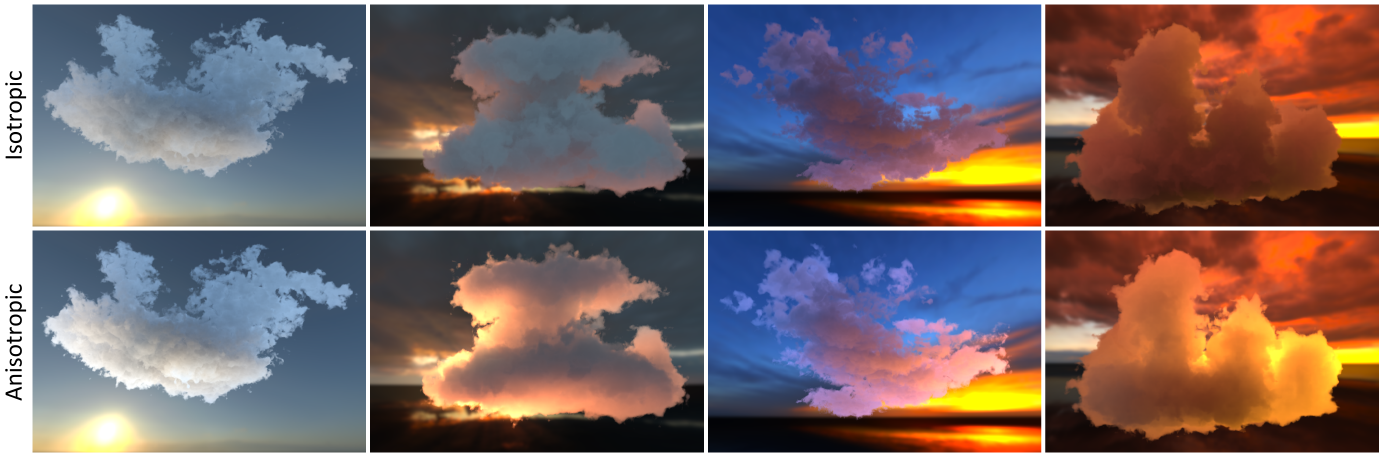

Figure 15: In media like clouds the scattering anisotropy plays a significant role in their appearance, thus the common assumption of isotropic scattering prevents a believable rendition of such media. The clouds are rendered by the described method at 35 Hz using 64 ordinates and 20^3 grid resolution for each of them, with 15 propagation iterations. The scattering anisotropy was set to $g = 0.96$.

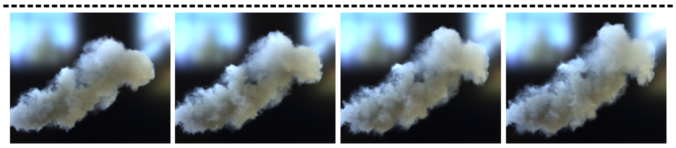

Figure 16: Animated sequence of an expanding smoke plume, rendered dynamically at 30 Hz by our method while maintaining good temporal coherence.

details). The employed empirical heuristics introduce a certain bias but allow us to make design decisions that result in a real-time performance on contemporary graphics hardware.

The decomposition into a finite number of directions for distant light can only be successful if the variation of the initial light distribution is not too high; this however holds for the HDR environment maps we used in our experiments (e.g. Fig. 15). In addition our prefiltered initialization can be used to avoid discretization artifacts in favour of a smooth approximation (Fig. 6).

Since the presented method directly relates to DOM it shares some of its basic limitations, such as handling of (surface) boundaries. In volumes with high density gradients (close to opaque surfaces) the light distribution might not be faithfully reproduced by the HG basis aligned with the initial light direction. Also the resolution of every principal grid is limited and the general limitations of discrete sampling apply: for finer details higher resolutions are required. However, the upsampling (Sec. 4.4) and prefiltering (Sec. 5.1) steps help to defer these issues and for typical volume data sets moderate propagation grid resolutions of 8^3–20^3 have shown to be sufficient to handle a wide range of illumination conditions and medium properties.

Another characteristic inherent to all finite-element methods is that their convergence rate depends not only on the propagation domain resolution but also on the optical thickness of the simulated medium; especially for high-albedo media the number of iterations required for producing a converged solution might be prohibitively high. Our approach deals with this issue by using multiple superimposed, relatively small propagation grids, in which a low number of iterations is sufficient to propagate most of the radiant energy (cf. Fig. 8). Media with higher optical thickness also decrease the anisotropy of the propagated light faster, allowing us to switch to the cheaper isotropic propagation mode earlier (Sec. 5.4). The lighting frequencies resulting from the isotropic transport are by definition low and therefore a lower-resolution propagation domain is sufficient here as well.

As future work, we would like to extend our propagation to work with hierarchical or nested grids to handle higher details in media as well as illumination. In general, we believe that the effect of complex lighting on dynamic participating media is an exciting visual phenomenon that deserves more dedicated research, e.g. to better understand human perception of volumetric light or the artistic practice applied to depict it.

Acknowledgements. We would like to thank Anton Kaplanyan for inspiring discussions, Chuong Nguyen, Peter Vangorp and Yulia Gryaditskaya for reviewing early drafts of the article, and the anonymous reviewers for their valuable feedback.

[1] M. Billeter, E. Sintorn, and U. Assarsson. Real-time multiple scattering using light propagation volumes. In *Proc. I3D*, 2012.
[2] A. Bouthors, F. Neyret, N. Max, E. Bruneton, and C. Crassin. Interactive multiple anisotropic scattering in clouds. In *Proc. I3D*, 2008.
[3] S. Chandrasekhar. *Radiative transfer*. Dover Publications, 1960.
[4] C. Dachsbacher and M. Stamminger. Reflective Shadow Maps. In *Proc. I3D*, pages 203–213, 2005.
[5] O. Elek, T. Ritschel, C. Dachsbacher, and H.-P. Seidel. Interactive light scattering with principal-ordinate propagation. In *Proc. Graphics Interface*, 2014.
[6] O. Elek, T. Ritschel, A. Wilkie, and H.-P. Seidel. Interactive cloud rendering using temporally coherent photon mapping. *Computers & Graphics*, 36:1109–1118, 2012.
[7] T. Engelhardt and C. Dachsbacher. Epipolar sampling for shadows and crepuscular rays in participating media with single scattering. In *Proc. I3D*, 2010.
[8] T. Engelhardt, J. Novák, T.-W. Schmidt, and C. Dachsbacher. Approximate bias compensation for rendering scenes with heterogeneous participating media. *Comp. Graph. Forum*, 31(7):2145–2154, 2012.

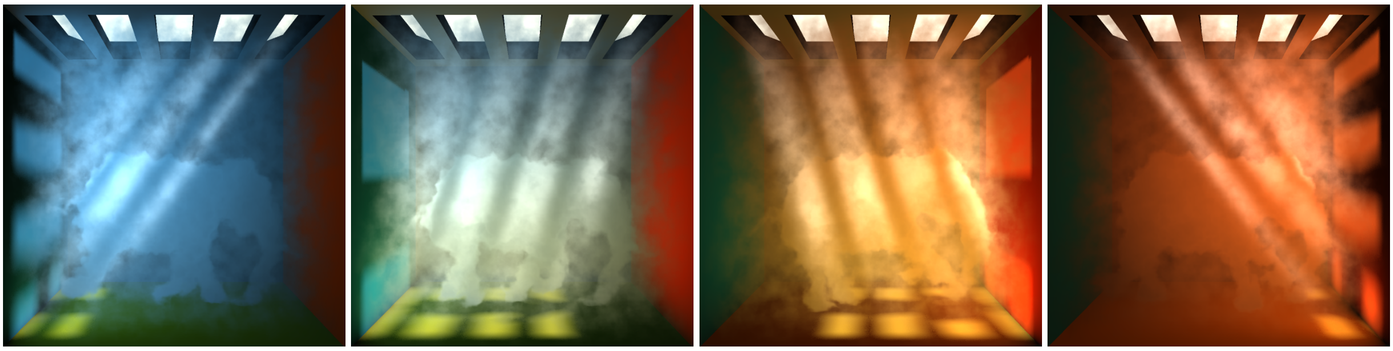

Figure 17: Scene with both animated medium and illumination, combining scattering from directional and local virtual light sources, running at 16 Hz (including the generation of the 125 VPLs and rendering the indirect illumination from surfaces, which alone takes 30 ms). The medium has a size of 20^3 m with $\sigma_s = \{3.2, 3.3, 3.4\}\,\mathrm{m}^{-1}$, $\sigma_a = \{1.15, 1.2, 1.3\}\,\mathrm{m}^{-1}$, $g = 0.7$, and is very heterogeneous. The grid size for the directional light is $128^2 \times 16$, with the 16-cell axis oriented along the light shafts (i.e. along the principal ordinate). The radial grids have a resolution of 8^3 each. We use these settings for local light sources in all our examples; note how even this small resolution proves to be sufficient for plausible results.

[9] R. Fattal. Participating media illumination using light propagation maps. *ACM Trans. Graph.*, 28:7:1–7:11, 2009.

[10] R. Geist, K. Rasche, J. Westall, and R. Schalkoff. Lattice-Boltzmann lighting. In *Proc. EGSR*, pages 355–362, 2004.

[11] L. G. Henyey and J. L. Greenstein. Diffuse radiation in the Galaxy. *Astrophysical Journal*, 93:70–83, 1941.

[12] W. Jarosz, C. Donner, M. Zwicker, and H. W. Jensen. Radiance caching for participating media. *ACM Trans. Graph.*, 27:7:1–7:11, 2008.

[13] W. Jarosz, D. Nowrouzezahrai, I. Sadeghi, and H. W. Jensen. A comprehensive theory of volumetric radiance estimation using photon points and beams. *ACM Trans. Graph.*, 30:5:1–5:19, 2011.

[14] H. W. Jensen and P. H. Christensen. Efficient simulation of light transport in scenes with participating media using photon maps. In *Proc. SIGGRAPH*, pages 311–320, 1998.

[15] A. Kaplanyan and C. Dachsbacher. Cascaded light propagation volumes for real-time indirect illumination. In *Proc. I3D*, 2010.

[16] A. Keller. Instant radiosity. In *Proc. SIGGRAPH*, pages 49–56, 1997.

[17] J. Kniss, S. Premože, C. Hansen, and D. Ebert. Interactive translucent volume rendering and procedural modeling. In *Proc. Visualization*, pages 109–116, 2002.

[18] J. Kopf, M. F. Cohen, D. Lischinski, and M. Uyttendaele. Joint bilateral upsampling. *ACM Trans. Graph*, 26(3):96, 2007.

[19] J. Krüger, K. Bürger, and R. Westermann. Interactive screen-space accurate photon tracing on GPUs. In *Proc. EGSR*, 2006.

[20] E. P. Lafortune and Y. D. Willems. Rendering participating media with bidirectional path tracing. In *Proc. EGWR*, pages 91–100, 1996.

[21] G. Liktor and C. Dachsbacher. Real-time volume caustics with adaptive beam tracing. In *Proc. I3D*, 2011.

[22] T. Lokovic and E. Veach. Deep shadow maps. In *Proc. SIGGRAPH*, pages 385–392, 2000.

[23] N. Max. Optical models for direct volume rendering. *IEEE Transactions on Visualization and Computer Graphics*, 1(2):99–108, 1995.

[24] N. Max, G. Schussman, R. Miyazaki, K. Iwasaki, and T. Nishita. Diffusion and multiple anisotropic scattering for global illumination in clouds. *J. WSCG*, 1–3:277–284, 2004.

[25] A. Musbach, G. W. Meyer, F. Reitich, and S. H. Oh. Full wave modeling of light propagation and reflection. *Comp. Graph. Forum*, 32(6), 2013.

[26] S. G. Narasimhan, M. Gupta, C. Donner, R. Ramamoorthi, S. K. Nayar, and H. W. Jensen. Acquiring scattering properties of participating media by dilution. *ACM Trans. Graph.*, 25:1003–1012, 2006.

[27] J. Novák, D. Nowrouzezahrai, C. Dachsbacher, and W. Jarosz. Progressive virtual beam lights. *Comp. Graph. Forum*, 31:1407–1413, 2012.

[28] J. Novák, D. Nowrouzezahrai, C. Dachsbacher, and W. Jarosz. Virtual ray lights for rendering scenes with participating media. *ACM Trans. Graph.*, 29(4):60:1–60:11, 2012.

[29] M. Pauly, T. Kollig, and A. Keller. Metropolis light transport for participating media. In *Proc. EGWR*, pages 11–22, 2000.

[30] E. Praun and H. Hoppe. Spherical parametrization and remeshing. *ACM Trans. Graph.*, 22(3):340–49, 2003.

[31] R. Prutkin, A. Kaplanyan, and C. Dachsbacher. Reflective shadow map clustering for real-time global illumination. In *Proc. Eurographics (Short Papers)*, pages 9–12, 2012.

[32] Z. Ren, K. Zhou, S. Lin, and B. Guo. Gradient-based interpolation and sampling for real-time rendering of inhomogeneous, single-scattering media. Technical report, Microsoft Research, 2008.

[33] H. E. Rushmeier and K. E. Torrance. The zonal method for calculating light intensities in the presence of a participating medium. *Computer Graphics (Proc. SIGGRAPH)*, 21:293–302, 1987.

[34] M. Salvi, K. Vidimče, A. Lauritzen, and A. Lefohn. Adaptive volumetric shadow maps. In *Proc. EGSR*, pages 1289–1296, June 2010.

[35] P. Sloan, J. Kautz, and J. Snyder. Precomputed radiance transfer for real-time rendering in dynamic, low-frequency lighting environments. In *ACM Trans. Graph.*, 2002.

[36] J. Stam. Multiple scattering as a diffusion process. In *Proc. EGWR*, pages 41–50, 1995.

[37] Y. Wang, J. Wang, N. Holzschuch, K. Subr, J.-H. Yong, and B. Guo. Real-time rendering of heterogeneous translucent objects with arbitrary shapes. *Comp. Graph. Forum*, 29:497–506, 2010.

[38] D. R. Wyman, M. S. Patterson, and B. C. Wilson. Similarity relations for the interaction parameters in radiation transport. *Applied Optics*, 28(24):5243–5249, 1989.

[39] K. Zhou, Z. Ren, S. Lin, H. Bao, B. Guo, and H.-Y. Shum. Real-time smoke rendering using compensated ray marching. In *ACM Trans. Graph.*, pages 36:1–36:12, 2008.